A versatile indirect detector design for hard X-ray microimaging

Paul-Antoine Douissard, Alexander Rack, Thierry Martin

*European Synchrotron Radiation Facility, Grenoble, France**

Angelica Cecilia, Thomas van de Kamp, Lukas Helfen, Tilo Baumbach

Karlsruhe Institute of Technology, Institute for Synchrotron Radiation – ANKA, Karlsruhe, Germany

Xavier Rochet, Xavier Chapel

*Optique Peter, Lentilly, France**

Linda Luquot

Centre Internacional de Mètodes Numèrics en Enginyeria, Institut de Diagnosi Ambiental i Estudis de l'Aigua, Barcelona, Spain

Xianghui Xiao

Advanced Photon Source, Argonne National Laboratory, Argonne, Illinois, USA

Jürgen Meinhardt

Fraunhofer-Institut für Silicatforschung ISC, Würzburg, Germany

(Dated: August 26, 2012)

Abstract

Indirect X-ray detectors are of outstanding importance for high resolution imaging, especially at synchrotron light sources: while consisting mostly of components which are widely commercially available, they allow for a broad range of applications in terms of the X-ray energy employed, radiation dose to the detector, data acquisition rate and spatial resolving power. Frequently, an indirect detector consists of a thin-film single crystal scintillator and a high-resolution visible light microscope as well as a camera. In this article, a novel modular-based indirect design is introduced, which **offers** several advantages: it can be adapted for different cameras, i. e. different sensor sizes, and can be trimmed to work either with (quasi-)monochromatic illumination and the correspondingly lower absorbed dose or with intense white beam irradiation. In addition, it allows for a motorized quick exchange between different magnifications / spatial resolutions. Developed within the European project SCIN^{TAX}, it is now commercially available. The characteristics of the detector in its different configurations (i. e. for low dose or for high dose irradiation) as measured within the SCIN^{TAX} project will be outlined. Together with selected applications from materials research, non-destructive evaluation and life sciences they underline the potential of this design to make high resolution X-ray imaging widely available.

Keywords: micro-tomography, high-resolution microscope, synchrotron instrumentation, coherent imaging, X-ray phase contrast, Synchrotron-CT, scintillator, single crystal film

*Corresponding authors' current address: P.-A. Douissard & A. Rack, ESRF, BP 220, 38043 Grenoble Cedex, France, e-mail: `paul_antoine.douissard@esrf.fr, arack@snafu.de`; Xavier Rochet, Optique Peter, Allée Romaine, ZA du Charpenay, 69210 Lentilly, France, e-mail: `info@optiquepeter.com`

I. INTRODUCTION

The use of indirect detection for X-ray imaging applications reaches back to the middle of the 1970s when the first systems were constructed in order to perform live-topography [12]: a phosphor screen converts the X-rays into visible light, visible light optics then project this luminescence image onto a camera. High resolution hard X-ray imaging using indirect detection schemes is a technique which was established at synchrotron light sources during the 1990s [4]. In combination with thin-film crystal scintillators, indirect detectors can reach a spatial resolving power close to the diffraction limit of the visible light emitted by the screen [21]. The intense photon flux density at synchrotron light sources, in combination with indirect X-ray detectors with high spatial resolution and high sensitivity, allows hard X-ray microimaging to be performed. When employed with tomography techniques, the imaging becomes three-dimensional [4]. Countless applications from such diverse scientific fields as materials research, biomedical imaging, paleontology, cultural heritage or life sciences underline the high value of synchrotron-based microimaging [2], [42], [51], [52], [36]. For laboratory-based X-ray sources indirect detectors are being used more and more, e. g. in non-destructive testing [48], [10].

The first commercially manufactured indirect high resolution imaging detector for synchrotron applications appeared at the end of the 1990s [45]. During the past ten years, various modified versions and further developments have been installed at synchrotron imaging stations, e. g. at the European Synchrotron Radiation Facility in France (e. g., beamlines ID19, ID22(NI)/NINA, [46], [26]), the tomcat beamline at the Swiss Light Source [41], at the BAM*line* at BESSY-II [34] and the TopoTomo beamline at ANKA [37] as well as at the **P06 station at PETRA III** [39] (Germany), the Shanghai Light Source (China), the Diamond Light Source (UK) and the Australian Light Source, cf. Fig. 1. Due to this success, a dedicated work package was included within a **Sixth** Framework Program of the European Commission project called SCIN^{TAX}, aiming to develop a modular indirect detection design which makes optimal use of a novel LSO-based (Lu_2SiO_5) scintillating material also developed within the project, cf. [8], [25], [5], [18].

Within this article, the modular design of the microscope in its different configurations as developed by the French company Optique Peter during SCIN^{TAX} will be introduced. Examples for theoretically achievable parameters will be given based on microscope objectives

and cameras currently in use for synchrotron imaging, such as the FReLoN CCD camera, type $2k$ [22]. The high versatility of the system will be further illustrated by characteristics of selected configurations measured at different imaging stations, ranging from extremely high flux and high energy radiation to the moderate flux of a bending magnet beamline. In addition, selected applications from materials research, non-destructive evaluation and life sciences will be shown.

II. TECHNICAL DESCRIPTION

The microscope design developed follows a modular approach, i. e. it can easily be modified to work with less aggressive illumination, such as monochromatic synchrotron radiation of moderate energy. Alternatively, high dose illumination such as polychromatic synchrotron hard X-ray radiation, or radiation with a higher energy range of up to several 100 keV or both is applicable as well, see Figs. 2 and 3 [30]. In order to allow for a high level of compatibility, a common camera support represents the backbone of the microscope. It accommodates a tube lens, an optional eyepiece (either a single one or a set of eyepieces for manual selection in order to trim the magnification for large sensor cameras), a motorized camera rotation, a camera mount and a flexible interface system. A so-called low-dose head or a high-dose head can be mounted to this common support. A wide range of cameras can be combined with the detector. F-mount, C-mount and specific mounts (e. g. for the FReLoN camera developed in-house at the European Synchrotron Radiation Facility (ESRF)) are supported. Microscope parts such as the camera head (rotation) and the objective head (focus motor as well as choice of the microscope objective) are frequently motorized. Adapter plates are available according to the specific needs of the customer, in order to facilitate easy installation in a given experimental configuration.

A. Low-dose configuration

The configuration suitable for low-dose applications and operating with outstandingly high spatial resolution follows the concepts introduced by Bonse and Busch [4]: a visible light microscope objective placed directly behind the scintillator captures the emitted luminescence light. A classical visible light microscope design with tube lens is then deployed

to project the scintillation image onto the sensor of a camera (cf. Fig. 3, left). Besides the common support, the configuration consists of a head that can accommodate up to three different microscope objectives from Olympus. This can be exchanged *in situ* via a revolver-like arrangement (cf. Fig. 2, inset (e); the common parameters are listed in Table I). The objective-revolver is fixed on a motorized platform that can be translated in order to focus the ensemble, i. e. to move the scintillator screen in the focal plane of the objective in use. The scintillator is mounted on a dedicated support which is placed as a cap atop the objective-carrier. It protects the fragile single-crystal thin-film scintillator and also enables the screens to be exchanged in an easy, reliable manner. A mirror, inclined at 45° with respect to the X-ray beam, is placed downstream of the objective-revolver. It reflects the light emitted by the scintillator onto the tube lens placed above (folded right-angle geometry of the optical beam path). The optional eyepiece (either a single one or an exchangeable set of eyepieces) is placed between the tube lens and the camera. It is used to adapt the magnification: by combining selected objectives and eyepieces, a wide range of magnifications is accessible (Table I). As a rule of thumb, large format cameras, i. e. chips with 2048 × 2048 pixels (pixel size of at least 9 µm) are combined with an eyepiece, small format cameras are not. Frequently, the configuration with an objective placed directly behind the scintillator would be used with moderate dose, i. e. the radiation transmitted by the scintillator does not cause irreversible damage to the visible light optics **nor does backscattered or fluorescence radiation deteriorate the spatial resolution**.

B. High-dose configuration

The concept used for high dose applications follows closely the original ideas for indirect detection as introduced by Hartmann et al. [12] (developed further by Koch et al. [20] in order to be compatible with high energy applications): long-working distance objectives placed outside the direct beam are deployed to capture the luminescence light from the scintillator. The microscope head is designed to operate in a configuration that can stand high-dose irradiation, it includes a scintillator support, a single long-working distance objective, again a mirror and a motorized focus (Fig. 3, right). The system is designed to withstand high flux X-ray irradiation and the corresponding heat load, and/or high energy irradiation up to several 100 keV. **Furthermore, in order to achieve high spatial resolution at these**

high X-ray energies it is required to have as less as possible scattering objects downstream of the scintillator. Working under such extreme conditions is beneficial for reaching high image acquisition rates [7, 38]. To achieve the required radiation hardness, the microscope objective does not directly face the X-ray beam, unlike the low-dose head. Instead, the mirror is placed at 45° with respect to the X-ray beam and reflects the light emitted by the scintillator directly onto the microscope objective, making an angle of 90° between the optical axis of the microscope and the X-ray beam. The objectives chosen are frequently supplied by Mitutoyo (Japan): infinity-corrected and therefore can be used in conjunction with a tube lens, which acts as a secondary lens to form the image. As for the low-dose setup, an optional eyepiece set is placed after the tube lens in order to select the overall optical magnification. Again, by combining different objectives with an eyepiece a wide range of magnifications can be chosen (see Table II).

In applications where the lateral extension (i. e. away from the beam axis) of the detector in one direction is a decisive parameter (e. g. in radiography with an inclined specimen plane or in synchrotron laminography [13]), this design can have further advantages. It eliminates the objective lens body / barrel from the x-ray optical axis and hence reduces the space needed perpendicular to the x-ray optical axis. The mirror, on the other hand, can be placed conveniently in such a way that the available numerical aperture is just covered to be reflected towards the objective lens. This means that there are almost no protruding parts (apart from the mirror edge) like the lens barrel or the lenses themselves towards the flat specimen. A design specifically adapted to these inclined geometries including laminographic imaging is presented in Fig. 4.

III. PERFORMANCE

The microscope configurations described in the previous section were tested under the realistic conditions of monochromatic as well as white beam synchrotron radiation using beamlines TopoTomo (ANKA light source, Germany), 2-BM (Advanced Photon Source (APS), USA) as well as BM05 and ID15a (ESRF, France) [19], [1], [9]. These beamlines have dissimilar characteristices, which allowed the optics to be commissioned under quite different configurations of X-ray energy spectra and photon flux densities.

The TopoTomo bending magnet beamline can work either in white beam or in monochro-

matic mode. The available white beam energy spectrum ranges between 1.5 keV and 40 keV with an integrated photon flux at the sample position of approximately 10^{16} photons/s (5 mm $\times$ 10 mm beam size). A monochromatic beam ranging between 6 keV and 40 keV is provided by a double-multilayer monochromator (two coatings available: W/Si, Pd/B_4C) with an energy resolution of approximately 1.5% and a photon flux density of around 5×10^{10} photons/s/mm^2 (between 10 keV and 20 keV) [37].

The X-ray spectrum and flux at the insertion device beamline ID15a is much harder and more intense than the TopoTomo beam. The asymmetric multipole wiggler provides a white beam energy spectrum between 44 keV and 500 keV with an X-ray photon flux density of approximately 10^{15} photons/mm^2/s when a 25 mm-thick silicon absorption filter is used [9], [35].

The bending magnet beamline BM05 was used with a double-crystal silicon monochromator [53]. The results allow for comparing the performance of the microscope in its low-dose configuration with very narrow energy bandwidth of $\Delta E/E \approx 10^{-4}$ (BM05) compared to the broad bandwidth illumination (TopoTomo).

Finally, the bending magnet beamline 2-BM was used with a double-multilayer monochromator (1.5% energy resolution) [44]. The resulting flux density of 1.5×10^{12} photons/s/mm^2 (at 15 keV X-ray energy) represents a configuration somewhere between the extreme cases of ID15a (white beam mode) and TopoTomo (multilayer monochromator)/BM05 (crystal monochromator).

In the following sections, the details of the performed tests will be described. For a better overview, the results obtained at ANKA, the APS and at the ESRF as well as the low-dose and high-dose configuration are treated in separate paragraphs. **The aim of the following sections is not to give a systematic overview about available configurations of the detector design and their performances: they are rather depicting the versatility of the design as it can be trimmed for applications under very dissimilar working conditions.**

A. Low-dose configuration: contrast and spatial resolution

1. *Beamline BM05 (ESRF)*

The microscope in its low-dose configuration was characterized at the ESRF imaging, optics and metrology bending-magnet beamline **BM05** in Grenoble, France [53]. The ESRF light source was operated during the experiments in 16-bunch filling mode, i. e. 16 highly populated and equally spaced electron bunches were circulating in the storage ring. The electron beam intensity was 90 mA at maximum. The microscope was coupled to a CCD camera (PCO AG, Kelheim, Germany, type SensicamQE [32]) and tested under irradiation with monochromatic synchrotron X-rays of 18 keV photon energy (Si(111) crystal monochromator, primary and secondary slits of the beamline were set to a 2 mm × 2 mm opening). The SensicamQE is a 12bit interline-transfer CCD camera with 1376 × 1040 pixels (6.75 µm pixel size) and low readout noise ($4e^-$ rms). The camera operates with a maximum of 65% quantum efficiency at 500 nm wavelength and is therefore well suited for capturing light from scintillators emitting in the green spectral range such as the Tb-doped Lu_2SiO_5 (LSO:Tb) developed within SCIN^{TAX} and Ce-doped $Y_3Al_5O_{12}$ (YAG:Ce) [8], [24].

For the low-dose microscope configuration the influence of the single crystal film thickness on the spatial resolution of the detector was investigated: different LSO:Tb single crystal films with thicknesses ranging from 2.5 µm to 100 µm (all deposited on nominal 150 µm thick substrates) and microscope objectives with different numerical apertures (0.16, 0.4 and 0.75, respectively) were combined (2.5× eyepiece installed). The focal position was tuned manually and the exposure times were adapted to the different X-ray stopping powers of the thin film scintillators. The spatial resolution was determined by imaging an Xradia test pattern (type Xradia X500-200-30) fixed on a dedicated holder at a distance of 5 mm from the scintillator (detector entrance window). The holder was placed on a motorized stage allowing the target and the detector to be aligned, as well as the different tilts to be corrected.

For each optical configuration and scintillator thickness, the spatial resolution was measured via the grid of the Xradia X500-200-30 test pattern [49]: 10 dark images, 10 flat images and 10 images of the target were recorded. In order to suppress unwanted artifacts due to image noise, a mean over the 10 images was performed for the dark, flat and the images

with the object before applying standard bright field and dark field correction [47].

The contrast was calculated from the grid of the Xradia test pattern using the formula

$$Contrast = \frac{I_{max} - I_{min}}{I_{max} + I_{min}} \tag{1}$$

where I_{max} is the bright part of the grid and I_{min} is the dark part of the grid.

In theory, three main parameters will influence the spatial resolution limit of the detector: i) the effective pixel size, ii) the Rayleigh criterion determining the spatial resolution limit due to the visible light optics and iii) the scintillator thickness which should be adapted to the depth of field (DOF) of the microscope. As the thickness of the layer is varied, the best contrast achievable will be mainly limited for this study by the Rayleigh criterion but not by the sampling: in accordance with Shannon's theorem, twice the effective input pixel size was chosen to be much smaller than the Rayleigh criterion of the optics. For an NA = 0.16 (0.67 µm effective pixel size, 28 µm depth of field, 2.2 µm Rayleigh resolution limit), the achievable contrast increases with decreasing thickness of the active layer until approximately the DOF is reached. **As depicted in Fig. 5:** for thinner active layers the best contrast slightly degrades. A similar behavior is depicted for an NA = 0.4 (0.28 µm effective pixel size, 5 µm depth of field, 0.9 µm Rayleigh resolution limit**, cf. Fig. 6**): the contrast improves until the DOF is reached and then slightly degrades. For NA = 0.75 (0.14 µm effective pixel size, 1 µm depth of field, 0.5 µm Rayleigh resolution limit**, cf. Fig. 7**) the contrast improves with decreasing thickness but no active layer with a thickness below the DOF was tested.

One can note that the best contrast achieved is relatively low. In fact the thickness of the target's gold structures is 3 µm, i. e. at 18 keV, only approximately 68% of the X-rays are stopped. This effect artificially decreases the contrast. Indeed, the measurements do not depict the spatial resolution limit of the system but rather underline the influence of the scintillator thickness on the system response. Additionally, one can observe an increase of the contrast for all measurements as the active layer thickness approaches the DOF of the microscope objective. Strictly speaking, according to the Abbe theorem for visible light microscopy the contrast should remain constant once the layer thickness drops below the DOF. Especially in Fig. 5 a degradation of the contrast is notable. This effect can be ascribed to the fact that for thinner layers, the interaction of the X-rays with the substrate of the single-crystal thin film scintillator becomes more dominant, i. e. scattering or emission of

characteristic X-rays broaden the system's point-spread function.

2. Beamline TopoTomo (ANKA)

In order to verify our findings as well as to underline the capability of the detector design to operate under different experimental conditions, tests were also carried out at the TopoTomo beamline of the ANKA light source (Germany). The influence of the thickness of the scintillator thin film on the spatial resolution achievable was studied by measuring the modulation transfer function (MTF) [6]. The microscope was coupled to an interline transfer CCD camera (PCO AG, Kelheim, Germany, type pco.4000 [32]) with a 10× objective (NA = 0.40) and a 2.5× eyepiece, resulting in an effective pixel size of 0.4 µm. The chip of the pco.4000 operates with 4000 × 2672 pixels, each with a physical pixel size of 9 µm. The camera uses 14bit digitalization, and the peak quantum efficiency is located at around 500 nm (50%), again well suited to the emission of the LSO:Tb scintillator. The camera's technical specifications claim a full-well capacity of 60 000 electrons per pixel and electron read-out noise of 12 e-rms (slowest readout for highest dynamic range) leading to a dynamic range of 5 000:1 gray levels.

A double-multilayer monochromator was used to select the X-ray energy from the emitted broad spectrum of the bending magnet source. The MTF was calculated at energies of 12 keV and 24 keV from a line spread function (LSF) acquired through imaging a cleaved GaAs edge (**500 µm thick**). The LSF calculation is based on the slanted edge method, in which the edge itself is slightly tilted (5 − 10 **degrees**) with respect to the pixel array of the detector. The software code "Slanted Edge MTF" available as ImageJ plugin was deployed [28]. **Basically, the LSF is the derivative of the edge-response of the optical system. The MTF is then obtained from the LSF via the (discrete) Fourier transform. The width of the LSF is usually expressed as the Full-Width-at-Half-Maximum (FWHM). It is the width of the LSF at 50% of the maximum value.**

The optimal contrast is achieved when the active layer thickness approaches the depth of focus of the microscope objective [21]. In our configuration, the spatial resolution of the system is diffraction limited to 0.82 µm (Rayleigh criterion), and the depth of focus is approximately 7 µm. At 12 keV and for a layer thickness of between 5 µm and 10 µm, the

full-width-half-maximum (FWHM) of the LSF is found to be 0.85 µm. The MTF drops below 20% at a frequency which corresponds to a spatial structure of 0.85 µm size **/ 580 lp/mm** (cf. Fig. 8**, MTF values higher than 1 are artifacts related to imperfect flat-field corrections of the background**). The derived results are in excellent agreement with the theoretical resolution limit of 0.82 µm.

At 24 keV and for a layer thickness of between 5 µm and 10 µm, the FWHM(LSF) is found to be 1.0 µm. Here, 20% of the MTF corresponds to a spatial structure of 1.0 µm size **/ 500 lp/mm** (see Fig. 9). The MTF is slightly degraded compared to that at 12 keV.

The characteristics derived underline that also at synchrotron light sources with comparable moderate photon flux density, high spatial resolution can be reached in case appropriate detection systems are used. Furthermore, these results depict the degradation of the spatial resolution of an indirect detector when switching to higher X-ray energies: due to the higher penetration depth of X-ray photons in the scintillator screen, physical phenomena such as Compton scattering, fluorescence and potential parasitic luminescence increase, causing a degradation of the spatial resolution.

3. Beamline 2-BM (APS)

In order to test the low-dose configuration with a (quasi-)monochromatic photon flux density significantly higher than TopoTomo (operated with a multilayer monochromator) / BM05 (operated with a crystal monochromator), experiments were carried out also at the 2-BM imaging station of the APS [44]. When operated with a multilayer monochromotor the photon flux density available at 2-BM is approximately two orders of magnitude higher than that at the TopoTomo beamline.

The microscope in its low-dose configuration was used together with an interline transfer CCD camera (Photometrics, USA, type Coolsnap K4 [33]) with a 20× objective (NA = 0.75) and a 2.5× eyepiece, resulting in an effective pixel size of 0.15 µm (see also Fig. 1). The dimensions of the sensor are 2048 × 2048 pixels with a physical pixel size of 7.4 µm. The data sheet of the camera claims a full-well capacity per pixel of 30 000 electrons resulting in a dynamic range of 3 000:1 gray-levels.

In order to convert the X-ray photons into visible light a 6 µm-thick Tb-doped $Gd_3Ga_5O_{12}$(GGG:Tb) thin crystal film scintillator on top of an undoped GGG-substrate

was deployed. An X-ray photon energy of 15.4 keV was used to acquire images of an in-house fabricated X-ray test pattern consisting of horizontal and vertical line structures (**500 nm** gold deposited on a **300 nm** silicon nitride membrane). The test pattern was placed at a distance of 5 mm upstream of the scintillator. The structure width as shown in Fig. 10 is 0.5 µm, i. e. representing a 1.0 µm periodicity. A representative line profile plot shown as well allows one to estimate the contrast modulation to of the order of 50%. One can conclude that an outstandingly high spatial resolution clearly below 1.0 µm has been reached.

B. High-dose configuration: spatial resolution and radiation hardness

1. *Beamline TopoTomo (ANKA)*

For testing the high-dose configuration, TopoTomo was operated in white beam mode, i. e. the bending magnet spectrum was filtered with 1 mm of silicon only. The resulting broad spectrum has its maximum around 20 keV **with a bandwidth ΔE/E of approximately 75%**. The optical performances of the microscope were investigated by coupling it to a pco.4000 camera (see previous section for more technical details on the camera).

To investigate the quality of the X-ray detector, a 12 µm LSO:Tb scintillator was integrated into the imaging system. Images of the Xradia test pattern X500-200-30 were acquired with total magnification equal to **36**×. The effective pixel size corresponding to such magnifications is **0.25** µm (cf. Table II).

The numerical aperture of the 10× objective used is 0.28 which defines the resolution limit to 1.2 µm, according to the Rayleigh criterion. As depicted in Fig. 11, the smallest feature of the test pattern that can be resolved corresponds to **half a period** between 0.6 µm and 0.7 µm, the achieved spatial resolution ranges between 1.2 µm **(415 lp/mm)** and 1.4 µm **(355 lp/mm)** [6]. The detector operates in the high-dose configuration with moderate X-ray photon energies at a spatial resolution close to the diffraction limit of the visible light optics used.

2. Beamline ID15a (ESRF)

The microscope configured for high-dose irradiation was commissioned under the intense flux and hard wavelengths available at the ESRF beamline ID15a where an asymmetric multipole wiggler provides a white beam spectrum between 44 keV and 500 keV. The aim of the experiment was to study the effect of the radiation damage on the detector system. However the spatial resolution was not investigated as no high resolution test pattern is available for this hard wavelength range. The spectrum was filtered with 25 mm of silicon and 5 mm of copper. The beam dimensions were equal to 1 mm × 1 mm. To protect the CCD detector and the microscope from the Compton scattered X-rays (dominant at photon energies above 100 keV) the detector was shielded with 3 mm thick lead. During that experiment the microscope was optically coupled with the high resolution 14bit pco.4000 CCD camera (technical details of the camera can be found in section III A 2).

The most prominent effect that was observed during the tests at ID15a is the darkening of the objective due to the scattered radiation. The corresponding decrease of the effective count rate under constant illumination was investigated by using a 15 µm thick LSO:Tb scintillator deposited on a 175 µm YbSO substrate The count rate decrease was estimated to be around 7.2%/hour. This count rate decrease is a combination of the radiation damage caused to the scintillator, the substrate, the microscope objective and the optics. (The Compton scattering contribution can be neglected at energies lower than 100 keV but it gets significant as the energy increases. For YAG, for example, the Compton probability is equal to 1.2% at 30 keV and 85% at 300 keV [24].)

By positioning a 4 mm lead glass (**30% lead concentration, 1.6 refractive index**) shielding between the microscope mirror and the objective, the count rate decrease was reduced, down to 0.6%/hour. In order to verify the best position for the protective lead glass, different optical configurations were investigated by changing the objective, the mirror and the lead glass sites within the system. For every arrangement, we acquired a visible light image of a JIMA-RT-RC-0 pattern and calculated its contrast according to equation (1) shown in paragraph III A 1.

The four configurations were: (a) microscope without mirror, (b) microscope with mirror, (c) microscope with mirror plus lead glass before the mirror (d) microscope with mirror plus lead glass between mirror and objective. The calculated values of the contrast were equal

to (a) 0.48+/-0.3, (b) 0.50+/-0.3, (c) 0.33+/-0.3 and (d) 0.51+/-0.3. They demonstrated the equivalence of configurations (a), (b) and (d). By contrast, the configuration in which the lead glass is located before the mirror is not favorable. **As the spatial resolution of an indirect detector is determined by the scintillator screen and the spatial resolving power of the visible light system used to capture its image: one can assume that the best given visible light optical configuration will as well reach the best spatial resolution in combination with X-rays and a given scintillator. Furthermore, only configuration (d) positions the lead glass where it does not interact with the X-rays and therefore, cannot act as scatterer or fluorescence source. Hence, only this configuration is well adapted for high-resolution X-ray imaging.**

The final version of the white beam microscope is usually equipped either with a 2× or 5× magnifying objectives for achieving intermediate resolution values equal to 6.1 µm and 2.4 µm, respectively. The optical data for those configurations are listed in Table II.

IV. APPLICATIONS

Hard X-ray microtomography is a popular analytical tool available at synchrotron light sources around the globe. This chapter outlines the potential of the versatile detector design introduced here for synchrotron-based microimaging by selected applications in such diverse fields as biology, geology, non-destructive evaluation and materials research. The examples give an impression of the high level of flexibility reached with the modular detector design described in this article.

A. High-contrast microtomography

Microtomography in combination with synchrotron radiation is frequently deployed where high spatial resolution, high contrast or both are required. As an example application, studying the microstructure of a fibre reinforced C/SiC ceramic was chosen [34], [40]. The sample is delicate as four different material phases have to be distinguished: silicon, carbon, silicon carbide and pores/cracks. Characteristics of these phases such as volume fraction and specific surface are required for optimizing the processing of C/SiC ceramics where, e. g.

cracks can occur which deteriorate the desired performance of the material.

For the experiment, the microscope in the low-dose configuration was used. The scintillator screen consisted of a single-crystal thin film of GGG:Eu (20 µm thick) on top of an undoped GGG substrate. The objective in use was a 5× (0.15 NA) combined with a 2.5× eyepiece. The ESRF inhouse camera FReLoN (type $e2v$) was used, leading to an effective pixel size of the detector of 1.1 µm. The sample was illuminated by an X-ray photon beam with a mean energy around 18 keV delivered by a single-harmonic undulator at the ESRF beamline ID19 [46]. The sample-detector distance was set to 9 mm and 1500 projection images were recorded during the tomographic scan.

A tomographic slice of a C/SiC sample acquired with these parameters is depicted in Fig. 12 (top). Three material phases have been marked, the fourth phase is visible as cracks throughout the sample. In order to verify the contrast achieved in the images (a mixture between classical absorption contrast and in-line X-ray phase contrast) a comparable sample has been imaged by scanning-electron microscopy, cf. Fig. 12 (bottom).

B. Rapid *in situ* microtomography

To characterize *in situ* dynamic structural parameters of rock samples during chemical reaction, fast data acquisition rates and X-ray imaging with microresolution are required. Because of the multi-phase composition of a rock sample, furthermore high image contrast is needed. Here the kinetics of calcite dissolution controlled by diffusion transport and the role of microstructure was studied. Dissolution processes involve complex coupled mechanisms, strongly controlled by the hydrodynamical and chemical variability of the system at all scales [23]. High spatial resolution scale is necessary to investigate fine grain material and to interpret hydrodynamic modifications on a large scale. The main focus is set on the multiscale distribution, interconnection and continuity of large primary or secondary pores which generally act as good percolation pathways during dissolution processes [11].

Experiments were carried out at ESRF beamline ID19. The high-resolution X-ray imaging system used comprised a FReLoN CCD camera and the microscope in its low-dose configuration. The latter was equipped with a 4× Olympus

objective and a 2× eyepiece. In order to reach higher data acquisition rates, the FReLoN camera was operated in the so-called FTM (Frame Transfer Mode) mode and with a pixel binning mode combined with a ROI (Region Of Interest), giving 512 × 512 pixels per image. The effective pixel size of the detector was 3.5 µm, giving a spatial resolution limit of R > 7 µm, according to Shannon's theorem. For the high resolution tomography scan an X-ray photon energy of 34 keV was selected by the beamline's single-bounce multilayer monochromator (Ru/B_4C coating). Two undulator insertion devices were combined. The sample-to-detector distance was 15 mm and 400 projection images were acquired by rotating the sample stepwise over 180°. With an exposure time of 0.035 s per image the scan acquisition lasted 17.8 s with a total acquisition time of 57.1 s (including overheads, flat field and dark field images). The three-dimensional images of the rock sample were reconstructed by using the filtered backprojection algorithm via the ESRF software package PyHST [27].

A pure calcite core sample of 2 mm diameter and 3 mm length with two different porosity structures (macro- and micro-porosity) was studied. In Fig. 13, one can observe the three-dimensional reconstruction of the rock sample at different times during the acidic attack (t0: initial stage, t30 = 28 min and t70 = 66 min). The macroporosity (in black) increases from 9.6% to 34.7% after 66 min of the experiment whereas the microporosity (in orange) decreases from 42.3% to 34.9% during the first 28 min and then increase up to 48.2% after 66 min of treatment. The increase of the dissolution rate during the experiment can be explained by the development of macro-pores which allow a better accessibility and penetration of the acidic fluid. This high speed and high resolution tomography approach opens new possibilities for structural characterization during in situ reaction processes.

C. White beam microtomography

In this section a microtomography application deploying white beam illumination is described that was accomplished at the TopoTomo beamline (ANKA) by using the high-dose configuration. The aim of the experiment was to reconstruct the morphology of a weevil

(*Trigonopterous*) through phase sensitive X-ray imaging.

For the experiment the beamline was operated in white beam mode. The emitted radiation was filtered with a silicon wafer of 1 mm thickness; the resulting energy spectrum had its peak around 20 keV with a bandwidth of approximately 75%. The tomography scan was performed with a high speed CMOS camera (Photron Japan, type SA-1), whose highest achievable data rate is equal to 5400 images/s in full frame mode. The scintillator used is a Ce-doped $Lu_3Al_5O_{12}$ (LuAG:Ce) crystal with thickness equal to 300 µm. The projection images were acquired with a total magnification of 3.6× (Mitutoyo objective 2×/NA = 0.055 and eyepiece 2×). The effective pixel size was equal to 5.6 µm and the propagation distance between sample and detector was set to 30 cm. A complete tomography scan (1500 projections) was recorded in 30 s by setting the detector frame rate to 50 images/s. To reconstruct the phase maps prior to the tomographic reconstructions, the ANKAphase phase-retrieval tool was used, that can be applied despite illuminating the sample with polychromatic synchrotron light [47], [31].

Due to their often hard and stiff exoskeletons, many insects are difficult to examine by classical morphological methods. Although scanning electron microscopy provides high resolution, internal structures remain hidden. Light- and transmission electron microscopy require slicing the samples, a process drastically altering their condition. Moreover, insect cuticle is particularly difficult to slice and tends to fracture in the process. As synchrotron-based hard X-ray microtomography allows non-destructive imaging of millimeter-sized objects, it became a powerful tool for entomologists. Virtual slices through the specimen allow taking a look at anatomical details. Additionally, the resulting data can be used to create digital three-dimensional models very useful for morphological and anatomical research [3]. **The volume rendering of the *Trigonopterus* weevil is depicted in Fig. 14 and the morphological details of the insect are reported in Fig. 15. The quality of the image is excellent, despite the use of polychromatic radiation.** The description of the weevil hip joint as a biological screw-and-nut system based on synchrotron x-ray microtomography data of thick-shelled *Trigonopterus* weevils demonstrates the potential of the technique for examining the functional morphology of small biological specimens when conventional methods are not an option [17]. The use of polychromatic hard radiation in combination with phase-retrieval techniques allows acquisition of highly sensitive images of delicate samples in short scan times. As the objects are almost transparent at the wave-

lengths in use, reduction of the dose to the sample is achieved as well.

D. White beam microlaminography

A promising application of the high dose-rate configuration exists for synchrotron-radiation computed laminography (SRCL). This 3D imaging technique [13] allows regions of interest on large, flat specimens to be investigated non-destructively. SRCL has originally been developed for inspection of microsystem and microelectronic devices [14] but has recently also found very interesting applications in materials science, paleontology, life sciences and cultural heritage studies. It can be understood as a generalisation of CT where the rotation axis is inclined at an angle smaller than 90° with respect to the beam direction [16]. With the specimen approximately aligned perpendicular to the rotation axis the projected specimen thickness and thus the (integral) transmission to the 2D detector remains approximately constant during a scan. This ensures reliable projection data in the acquisition process and often results in 3D images with less artifacts than for limited-angle CT [50].

Depending on the beamline lay-out, synchrotron radiation can be partially coherent. Absorption imaging therefore requires one to minimise the distance between the 2D detector and the specimen which remains challenging for the SRCL data acquisition geometry. Also for optimised laminographic phase-contrast imaging [15] it is sometimes necessary to have small propagation distances between the sample and the detector, especially for spatial resolutions around 1 µm. The design proposed in Fig. 4 allows one to better accommodate for these necessities since in one direction with respect to the x-ray optical axis the detector can be designed rather compact.

Fig. 16 shows an example of a flip-chip bonded device where laminographic phase-contrast imaging at a single rather low propagation distance of around 40 mm was employed. The experiment was carried out at the ESRF beamline ID19 in white-beam mode with the peak of the energy distribution absorbed by the scintillator above 60 keV. Using an ESRF FReLoN 2k camera and 18× total magnification (10× Mitutoyo objective and 2× eyepiece) an effective pixel size of 0.8 µm was chosen. Due to the high energy spectrum employed, a GGG:Eu scintillator of 30 µm thickness on a substrate was selected. The cross-sectional slice at the interface between bump bonds and metallisation on the printed circuit board

was reconstructed from 2000 projection radiographs (exposure time 0.6 s each). A slight edge enhancement effect due to phase contrast is visible around the different materials. The microstructure of the Cu metal lines is clearly visible and voids are found in the bump bonds at the interface. We see that such 3D images give insight into the (visually not accessible) interconnects which is an important information for improving the interconnection technology and fine-tuning of production parameters. Furthermore, the behaviour of the interconnects under different loading conditions (e. g. temperature and / or electrical current) can be observed [43].

V. SUMMARY

The modular indirect detector design developed within the SCIN^{TAX} project has been introduced in this article and typical application cases described. Its low-dose configuration has been proven to reach outstanding spatial resolution in X-ray imaging. A further gain in resolving power can be achieved when the detector is operated together with magnifying X-ray optics [26]. The high-dose configuration has been successfully used under the intense radiation of a bending magnet source and a wiggler insertion device. Frequently, both configurations are operated with protective lead glass between the scintillator and the front lens of the microscope objective. Nevertheless, darkening of the objective is typically still prominent after longer use but can be cured with UV illumination.

Several aspects have not been considered in the article but need to be mentioned: the accuracy of the mechanics as well as the surface quality of scintillators is limited. It is therefore recommended always to operate high-resolution indirect detectors with scintillator mounts which allow for tilt compensation. When equipped with a thin free-standing scintillator and a thin mirror, the high-dose head allows one to to operate to a certain extent in a semitransparent manner. A second detector downstream of the high-dose system can then be used as well, e. g. for collecting diffraction signals.

The indirect design is available to the X-ray imaging community. It is the aim and hope of the authors that X-ray synchrotron imaging will benefit from the improvements brought by the high-resolution X-ray detector developed within the SCIN^{TAX} project.

Acknowledgments

The SCIN^{TAX} project is funded by the European community (STRP 033 427) as part of the Sixth Framework Programme (FP6). We thank Eric Ziegler, scientist in charge of the ESRF beamline BM05, for giving us the opportunity to test the X-ray detector presented. We thank Feng Xu and Yin Cheng (ANKA) for help with the data acquisition at beamline ID19, Tian Tian (University of California Los Angeles, U.S.) for providing the device for the laminography example, and **Gerald Falkenberg (DESY) for the photo of the microscope at P06 of PETRA III**. Use of the Advanced Photon Source, an Office of Science User Facility operated for the U.S. Department of Energy (DOE) Office of Science by Argonne National Laboratory, was supported by the U.S. DOE under Contract No. DE-AC02-06CH11357. Technical support during the experiment at 2-BM by Pavel Shevchenko (APS) is acknowledged **as well as Joan Vila-Comamala (APS) for providing the X-ray test pattern**. Beamtime at ID15a was provided by the European Synchrotron Radiation Facility (MI935). Support and fruitful discussions with Mathew Peele and Tamzin Lafford (ESRF), Patrik Vagovic and Tomy dos Santos Rolo (ANKA) are acknowledged as well. Alexander Rack acknowledges financial support by the X-Ray Science Division (XSD) Visitor Program of the Advanced Photon Source.

---

[1] Advanced Photon Source (2012). *Advanced Photon Source*. http://www.aps.anl.gov.

[2] Banhart, J., ed. (2008). *Advanced Tomographic Methods in Materials Research and Engineering*. Oxford University Press.

[3] Betz, O., Wegst, U., Weide, D., Heethoff, M., Helfen, L., Lee, W. & Cloetens, P. (2007). Imaging applications of synchrotron X-ray micro-tomography in biological morphology and biomaterial science. I. general aspects of the technique and its advantages in the analysis of arthropod structure. *J. Microsc.* **227**(1), 51–71.

[4] Bonse, U. & Busch, F. (1996). X-ray computed microtomography (μCT) using synchrotron radiation (SR). *Prog. Biophys. Molec. Biol.* **65**, 133–169.

[5] Cecilia, A., Rack, A., Pelliccia, D., Douissard, P.-A., Martin, T., Couchaud, M., Dupré, K. & Baumbach, T. (2009). Studies of LSO:Tb radio-luminescence properties using white beam

hard x-ray synchrotron irradiation. *Radiat. Effects Defect Solids* **164**(9), 517–522.

[6] Cecilia, A., Rack, A., Douissard, P.-A., Martin, T., dos Santos Rolo, T., Vagovic, P., Hamann, E., van de Kamp, T., Riedel, A., Fiederle, M. & Baumbach, T. (2011). LPE grown LSO:Tb scintillator films for high-resolution X-ray imaging applications at synchrotron light sources. *Nucl. Instr. & Meth. in Phys. Res. A* **648, Supplement 1**, S321–S323.

[7] Di Michiel, M., Merino, J. M., Fernandez-Carreiras, D., Buslaps, T., Honkimäki, V., Falus, P., Martins, T. & Svensson, O. (2005). Fast microtomography using high energy synchrotron radiation. *Rev. Sci. Instrum.* **76**, 043702–1–043702–7.

[8] Douissard, P.-A., Cecilia, A., Martin, T., Chevalier, V., Couchaud, M., Baumbach, T., Dupré, K., Kühbacher, M. & Rack, A. (2010). A novel epitaxially grown LSO-based thin film scintillator for micro-imaging using hard synchrotron radiation. *J. Synchrotron Radiat.* **17**, 571–583.

[9] European Synchrotron Radiation Facility (2012). *The synchrotron light source ESRF*. http://www.esrf.fr.

[10] Feser, M., Gelb, J., Chang, H., Cui, H., Duewer, F., Lau, S. H., Tkachuk, A. & Yun, W. (2008). Sub-micron resolution CT for failure analysis and process development. *Meas. Sci. Technol.* **19**(9), 094001.

[11] Gouze, P. & Luquot, L. (2011). X-ray microtomography characterization of porosity, permeability and reactive surface changes during dissolution. *J. Contaminant Hydrol.* **120–121**, 45–55.

[12] Hartmann, W., Markewitz, G., Rettenmaier, U. & Queisser, H. J. (1975). High resolution direct-display X-ray topography. *Appl. Phys. Lett.* **27**, 308–309.

[13] Helfen, L., Baumbach, T., Mikulík, P., Kiel, D., Pernot, P., Cloetens, P. & Baruchel, J. (2005). High-resolution three-dimensional imaging of flat objects by synchrotron-radiation computed laminography. *Appl. Phys. Lett.* **86**, 071915.

[14] Helfen, L., Myagotin, A., Rack, A., Pernot, P., Mikulík, P., Michiel, M. D. & Baumbach, T. (2007). Synchrotron-radiation computed laminography for high-resolution three-dimensional imaging of flat devices. *phys. stat. sol. (a)* **204**, 2760–2765.

[15] Helfen, L., Baumbach, T., Cloetens, P. & Baruchel, J. (2009). Phase-contrast and holographic computed laminography. *Appl. Phys. Lett.* **94**, 104103.

[16] Helfen, L., Myagotin, A., Mikulík, P., Pernot, P., Voropaev, A., Elyyan, M., Michiel, M. D., Baruchel, J. & Baumbach, T. (2011). On the implementation of computed laminography using

synchrotron radiation. *Rev. Sci. Instrum.* **82**(6), 063702.

[17] van de Kamp, T., Vagovic, P., Baumbach, T. & Riedel, A. (2011). A biological screw in a beetle's leg. *Science* **333**(6038), 52.

[18] Karlsruhe Institute of Technology (2012). *ScinTax – Novel ceramic thin scintillator for high resolution X-ray imaging*. http://www.scintax.eu.

[19] Karlsruhe Institute of Technology (2012). *The synchrotron light source ANKA*. http://ankaweb.fzk.de.

[20] Koch, A. (1994). Lens coupled scintillating screen-ccd X-ray area detector with a high quantum efficiency. *Nucl. Instr. & Meth. in Phys. Res. A* **348**, 654–658.

[21] Koch, A., Raven, C., Spanne, P. & Snigirev, A. (1998). X-ray imaging with submicrometer resolution employing transparent luminescent screens. *J. Opt. Soc. Am.* **15**, 1940–1951.

[22] Labiche, J.-C., Mathon, O., Pascarelli, S., Newton, M. A., Ferre, G. G., Curfs, C., Vaughan, G., Homs, A. & Carreiras, D. F. (2007). The fast readout low noise camera as a versatile x-ray detector for time resolved dispersive extended x-ray absorption fine structure and diffraction studies of dynamic problems in materials science, chemistry, and catalysis. *Rev. Sci. Instrum.* **78**, 0901301.

[23] Luquot, L. & Gouze, P. (2009). Experimental determination of porosity and permeability changes induced by injection of CO2 into carbonate rocks. *Chem. Geol.* **265**(1–2), 148–159.

[24] Martin, T. & Koch, A. (2006). Recent developments in X-ray imaging with micrometer spatial resolution. *J. Synchrotron Rad.* **13**, 180–194.

[25] Martin, T., Douissard, P.-A., Couchaud, M., Cecilia, A., Baumbach, T., Dupré, K. & Rack, A. (2009). LSO-based single crystal film scintillator for synchrotron-based hard x-ray micro-imaging. *IEEE Trans. Nucl. Sci.* **56**, 1412–1418.

[26] Martínez-Criado, G., Tucoulou, R., Cloetens, P., Bleuet, P., Bohic, S., Cauzid, J., Kieffer, I., Kosior, E., Labouré, S., Petitgirard, S., Rack, A., Sans, J. A., Segura-Ruiz, J., Suhonen, H., Susini, J. & Villanova, J. (2012). Status of the hard X-ray microprobe beamline ID22 of the European Synchrotron Radiation Facility. *J. Synchrotron Radiat.* **19**(1), 10–18.

[27] Mirone, A., Wilcke, R., Hammersley, A. & Ferrero, C. (last visit 2012). *PyHST – High Speed Tomographic Reconstruction*. http://www.esrf.eu/UsersAndScience/Experiments/TBS/SciSoft/.

[28] National Institutes of Health (2012). *ImageJ Slanted Edge MTF Plugin Web Site*.

http://rsbweb.nih.gov/ij/plugins/se-mtf/index.html.

[29] Noiriel, C., Luquot, L., Madé, B., Raimbault, L., Gouze, P. & Van Der Lee, J. (2009). Changes in reactive surface area during limestone dissolution: An experimental and modelling study. *Chem. Geol.* **265**(1–2), 160–170.

[30] Optique Peter (2012). *Optique Peter, ingénierie optique et mécanique*. http://www.optiquepeter.com.

[31] Paganin, D., Mayo, S. C., Gureyev, T. E., Miller, P. R. & Wilkins, S. W. (2002). Simultaneous phase and amplitude extraction from a single defocused image of a homogeneous object. *J. Microsc.* **206**, 33–40.

[32] PCO AG / The Cooke Cooperation (2012). *pco.4000 – cooled digital 14bit CCD camera system*. http://www.pco.de.

[33] PHOTOMETRICS (2012). *Photometrics CoolSNAP K4*. http://www.photometrics.com/products/ccdcams/coolsnap_k4.php.

[34] Rack, A., Zabler, S., Müller, B., Riesemeier, H., Weidemann, G., Lange, A., Goebbels, J., Hentschel, M. & Görner, W. (2008). High resolution synchrotron-based radiography and tomography using hard X-rays at the BAMline (BESSY II). *Nucl. Instr. & Meth. in Phys. Res. A* **586**(2), 327–344.

[35] Rack, A., García-Moreno, F., Baumbach, T. & Banhart, J. (2009). Synchrotron-based radioscopy employing spatio-temporal micro-resolution for studying fast phenomena in liquid metal foams. *J. Synchrotron Rad.* **16**(3), 432–434.

[36] Rack, A., Helwig, H.-M., Bütow, A., Rueda, A., Matijašević-Lux, B., Helfen, L., Goebbels, J. & Banhart, J. (2009). Early pore formation in aluminium foams studied by synchrotron-based microtomography and 3-D image analysis. *Acta Mater.* **57**(16), 4809–4821.

[37] Rack, A., Weitkamp, T., Bauer Trabelsi, S., Modregger, P., Cecilia, A., dos Santos Rolo, T., Rack, T., Haas, D., Simon, R., Heldele, R., Schulz, M., Mayzel, B., Danilewsky, A. N., Waterstradt, T., Diete, W., Riesemeier, H., Müller, B. R. & Baumbach, T. (2009). The microimaging station of the TopoTomo beamline at the ANKA synchrotron light source. *Nucl. Instr. & Meth. in Phys. Res. B* **267**(11), 1978–1988.

[38] Rack, A., García-Moreno, F., Schmitt, C., Betz, O., Cecilia, A., Ershov, A., Rack, T., Banhart, J. & Zabler, S. (2010). On the possibilities of hard x-ray imaging with high spatio-temporal resolution using polychromatic synchrotron radiation. *J. X-Ray Sci. Tech.* **18**, 429–441.

[39] Schroer, C. G., Boye, P., Feldkamp, J. M., Patommel, J., Samberg, D., Schropp, A., Schwab, A., Stephan, S., Falkenberg, G., Wellenreuther, G., Reimers, N. (2010). Hard X-ray nanoprobe at beamline P06 at PETRA III *Nucl. Instr. & Meth. in Phys. Res. A* **616**, 93–97.

[40] Shafei, B. & Steidl, G. (2012). Segmentation of images with separating layers by fuzzy c-means and convex optimization. *J. Vis. Commun. Image R.* **23**(4), 611–621.

[41] Stampanoni, M., Groso, A., Isenegger, A., Mikuljan, G., Chen, Q., Meister, D., Lange, M., Betemps, R., Henein, S. & Abela, R. (2007). Tomcat: A beamline for tomographic microscopy and coherent radiology experiments. In: *AIP Conference Proceedings (SRI2006)* (eds. J.-Y. Choi & S. Rah), vol. 879, 848–851.

[42] Stock, S. R. (2008). *MicroComputed Tomography: Methodology and Applications*. CRC Press, Boca Raton, FL, USA.

[43] Tian, T., Xu, F., Han, J. K., Choi, D., Cheng, Y., Helfen, L., Michiel, M. D., Baumbach, T. & Tu, K. N. (2011). Rapid diagnosis of electromigration induced failure time of Pb-free flip chip solder joints by high resolution synchrotron radiation laminography. *Appl. Phys. Lett.* **99**(8), 082114.

[44] Wang, Y., De Carlo, F., Mancini, D. C., McNulty, I., Tieman, B., Bresnahan, J., Foster, I., Insley, J., Lange, P., Laszewski, G., Kesselmann, C., Su, M.-H. & Thibaux, M. (2001). A high-throughput x-ray microtomography system at the Advanced Photon Source. *Rev. Sci. Instrum.* **72**(4), 2062–2068.

[45] Weitkamp, T., Raven, C. & Snigirev, A. A. (1999). Imaging and microtomography facility at the ESRF beamline ID 22. In: *Developments in X-ray Tomography II* (ed. U. Bonse), volume 3722 of *Proc. of SPIE*, 311–317.

[46] Weitkamp, T., Tafforeau, P., Boller, E., Cloetens, P., Valade, J.-P., Bernard, P., Peyrin, F., Ludwig, W., Helfen, L. & Baruchel, J. (2010). Status and evolution of the ESRF beamline ID19. *AIP Conf. Proc.* **1221**, 33–38.

[47] Weitkamp, T., Haas, D., Wegrzynek, D. & Rack, A. (2011). *ANKAphase*: software for single-distance phase retrieval from inline X-ray phase-contrast radiographs. *J. Synchrotron Radiat.* **18**(4), 617–629.

[48] Withers, P. J. (2007). X-ray nanotomography. *Materials Today* **10**(12), 26–34.

[49] Xradia Inc. (2012). *Xradia*. http://www.xradia.com/.

[50] Xu, F., Helfen, L., Baumbach, T. & Suhonen, H. (2012). Comparison of image quality in

computed laminography and tomography. *Opt. Express* **20**(2), 794–806.

[51] Zabler, S., Rueda, A., Rack, A., Riesemeier, H., Zaslansky, P., Manke, I., García-Moreno, F. & Banhart, J. (2007). Coarsening of grain-refined semi-solid Al-Ge32 alloy: X-ray microtomography and in situ radiography. *Acta Mater.* **55**(15), 5045 – 5055.

[52] Zabler, S., Rack, A., Manke, I., Thermann, K., Tiedemann, J., Harthill, N. & Riesemeier, H. (2008). High-resolution tomography of cracks, voids and micro-structure in greywacke and limestone. *J. Struct. Geol.* **30**(7), 876 – 887.

[53] Ziegler, E., Hoszowska, J., Bigault, T., Peverini, L., Massonnat, J. Y. & Hustache, R. (2004). The ESRF BM05 metrology beamline: Instrumentation and performance upgrade. In: *Proc. of SRI03* (eds. T. Warwick, J. Stohr, H. A. Padmore & J. Arthur), vol. 705 of *AIP Conf. Proc.*, 436–439.

TABLE I: Example parameters of the microscope in low-dose configuration, combined with cameras widely used in synchrotron imaging.

Olympus objective: magnification	4×	10×	20×	40×
Eyepiece: magnification	2.5×	2.5×	2.5×	2.5×
Total magnification	10×	25×	50×	100×
Numerical aperture (NA)	0.16	0.40	0.75	0.95
Working distance [mm]	13.0	3.1	0.6	0.18
Rayleigh resolution limit [µm]	2.2	0.9	0.5	0.4
pco.4000 CCD, 4008 × 2672 pixels, 9.0 µm pixel size				
Hor. objective field [mm]	3.6	1.4	0.72	0.36
Vert. objective field [mm]	2.4	1.0	0.48	0.24
Hor. effective pixel size [µm]	0.9	0.4	0.18	0.09
Vert. effective pixel size [µm]	0.9	0.4	0.18	0.09
pco.2000 CCD camera, 2048 × 2048 pixels, 7.4 µm pixel size				
Hor. objective field [mm]	1.5	0.6	0.3	0.15
Vert. objective field [mm]	1.5	0.6	0.3	0.15
Hor. effective pixel size [µm]	0.74	0.33	0.15	0.075
Vert. effective pixel size [µm]	0.74	0.33	0.15	0.075
FReLoN CCD camera, type $2k$, 2048 × 2048 pixels, 14.0 µm pixel size				
Hor. objective field [mm]	2.9	1.3	0.6	0.28
Vert. objective field [mm]	2.9	1.3	0.6	0.28
Hor. effective pixel size [µm]	1.4	0.6	0.28	0.14
Vert. effective pixel size [µm]	1.4	0.6	0.28	0.14

TABLE II: Example parameters of the microscope in high-dose configuration, combined with cameras widely used in synchrotron imaging.

Mitutoyo objective: magnification	2×	5×	5×	10×	10×	10×
Eyepiece	2.5×	2.5×	3.3×	2.5×	3.3×	4×
Total magnification	4.5×	11.25×	14.85×	22.5×	29.7×	36×
Numerical aperture (NA)	0.055	0.14	0.14	0.28	0.28	0.28
Working distance [mm]	34	34	34	33	33	33
Resolution limit [µm]	5.55	2.18	2.18	1.09	1.09	1.09
pco.4000 CCD, 4008 × 2672 pixels, 9.0 µm pixel size						
Hor. objective field [mm]	8.0	3.2	2.4	1.6	1.2	1.0
Vert. objective field [mm]	5.3	2.1	1.3	1.1	0.8	0.6
Hor. effective pixel size [µm]	2	0.8	0.6	0.4	0.3	0.25
Vert. effective pixel size [µm]	2	0.8	0.6	0.4	0.3	0.25
pco.2000 CCD camera, 2048 × 2048 pixels, 7.4 µm pixel size						
Hor. objective field [mm]	3.3	1.3	1.0	0.7	0.5	0.4
Vert. objective field [mm]	1.3	1.3	1.0	0.7	0.5	0.4
Hor. effective pixel size [µm]	1.6	0.6	0.5	0.3	0.25	0.2
Vert. effective pixel size [µm]	1.6	0.6	0.5	0.3	0.25	0.2
FReLoN CCD camera, type $2k$, 2048 × 2048 pixels						
14.0 µm pixel size						
Hor. objective field [mm]	6.4	2.5	1.9	1.3	0.9	0.8
Vert. objective field [mm]	6.4	2.5	1.9	1.3	0.9	0.8
Hor. effective pixel size [µm]	3.1	1.24	0.94	0.62	0.47	0.39
Vert. effective pixel size [µm]	3.1	1.24	0.94	0.62	0.47	0.39

FIG. 1: [1.5-column-span] Different incarnations of indirect detector microscopes for hard X-ray microimaging by the French company Optique Peter (Lentilly). From left to right: the very first system, installed at the ESRF beamline ID22, a modified version with a long nose for short sample-detector distances (TopoTomo beamline at ANKA, Germany), the modular design in its white beam configuration (beamline ID19, ESRF), a modular system in monochromatic configuration (beamline 2-BM of the Advanced Photon Source, USA) **and a monochromatic system with single eyepiece (beamline P06 of PETRA III, Germany)**. See also Figs. 2 and 3.

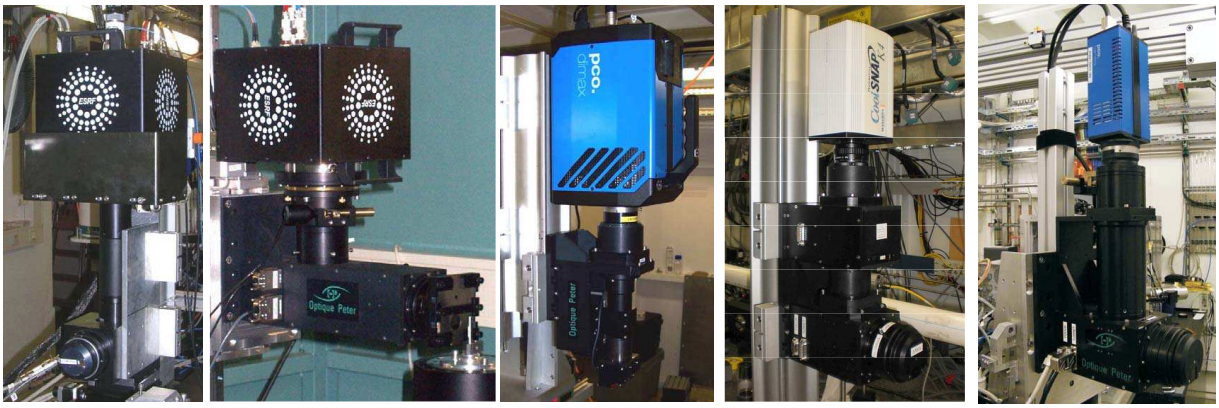

FIG. 2: [1.5-column-span] Main components of the modular indirect detector: a) the common support with tube lens and (optional) eyepiece box (b) with four positions. (Alternatively, the detector can operate without an eyepiece, or with a single permanent eyepiece installed, neither of which is shown in the sketch). (a) can be combined with the low-dose head (c) or the high-dose head (d). The inset (e) shows a sketch of the frontal view of the low-dose head (left) as well as a photo of the head without scintillator mount (right), giving a view into the revolver-mount with three microscope objectives. Further details and the optical beam paths are depicted in Fig. 3.

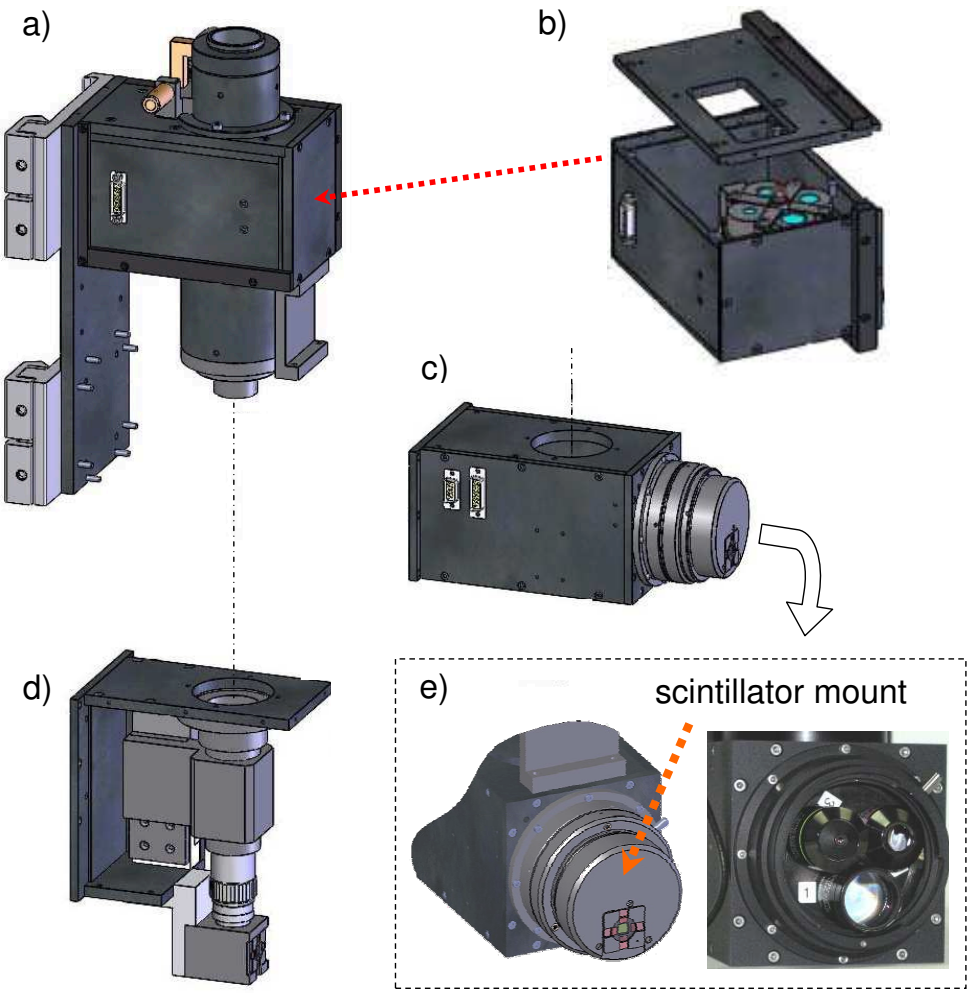

FIG. 3: [1.5-column-span] The indirect detector microscope in two standard configurations. Left: low-dose configuration with eyepiece box, the optical beam path is sketched below. Right: high-dose configuration with eyepiece box. The main difference between the two settings: for the high-dose configuration, no optics are placed behind the scintillator, so no optics are exposed to the direct beam.

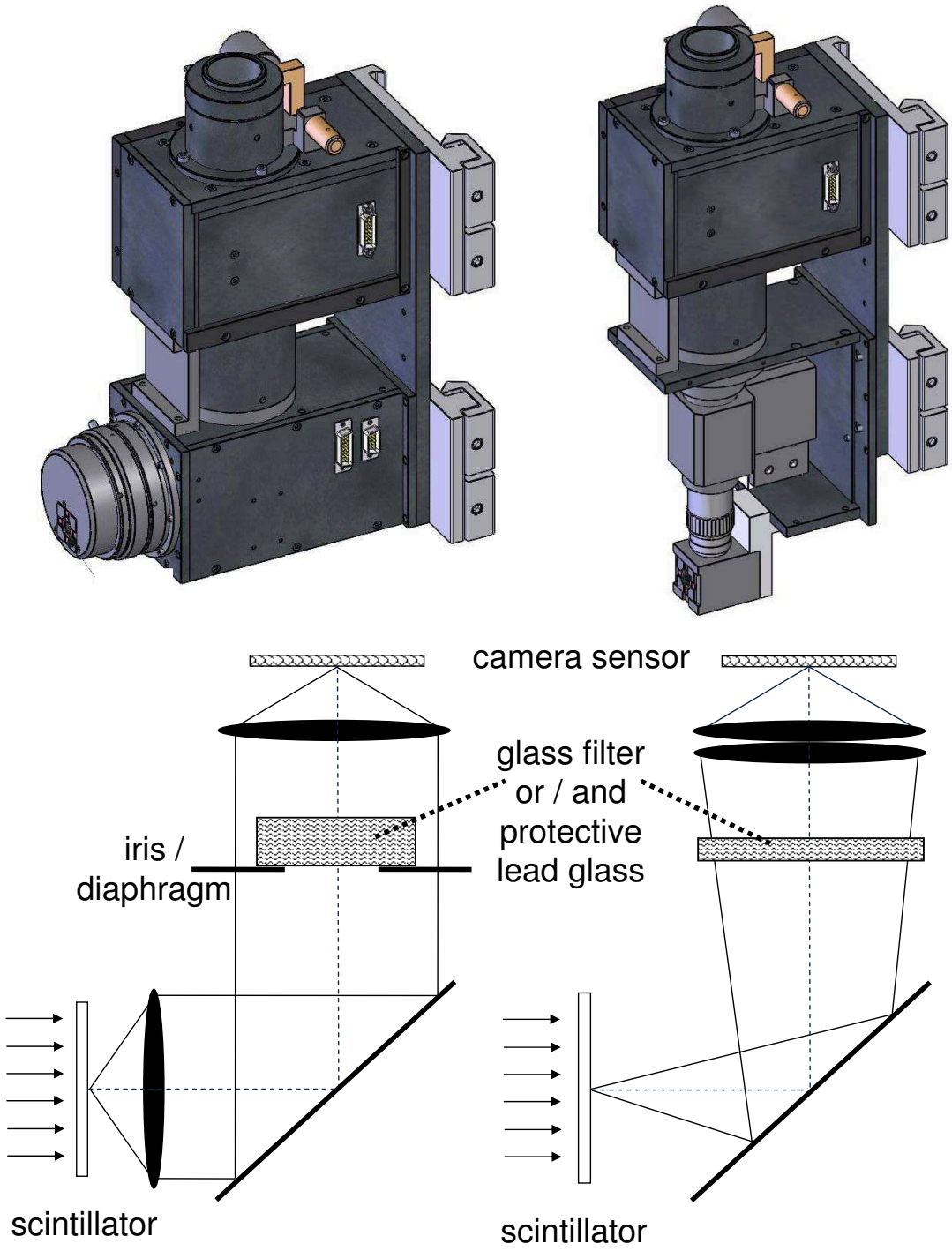

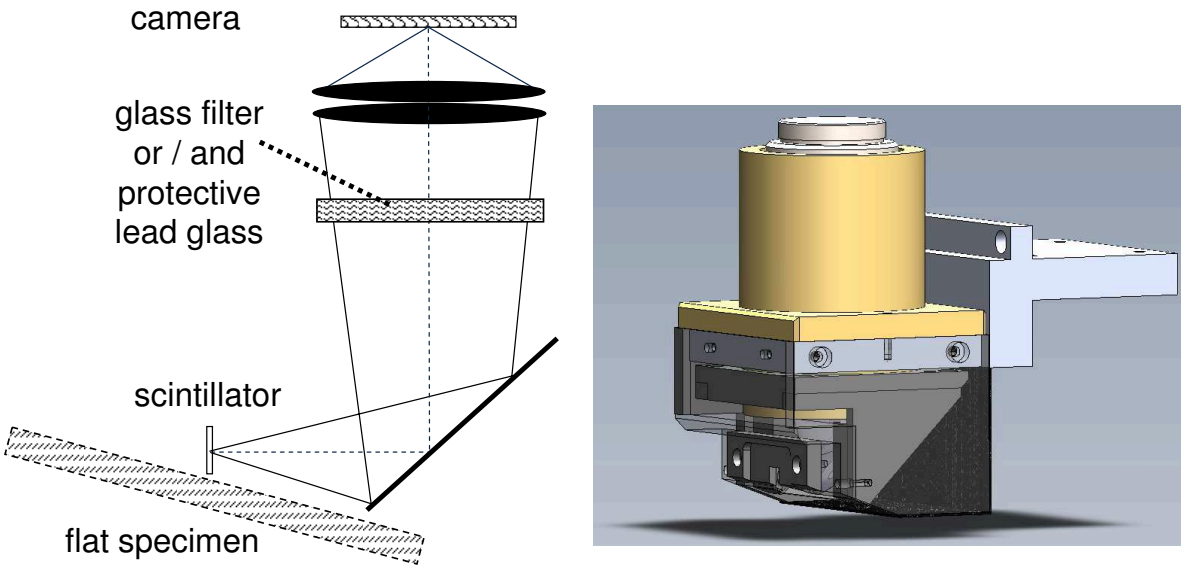

FIG. 4: [1-column-span] Left: optical beampath of the indirect detector microscope in its high-dose rate configuration adapted to flat specimens and inclined geometries, right: the corresponding modified section of the high-dose head, cf. Fig. 2 (d).

FIG. 5: [1-column-span] Influence of the thickness of the single crystal scintillator film on the contrast achievable in the image with a 4× (NA = 0.16) microscope objective (18 keV photon energy, different graphs represent results obtained by using differently sized features in the Xradia test pattern).

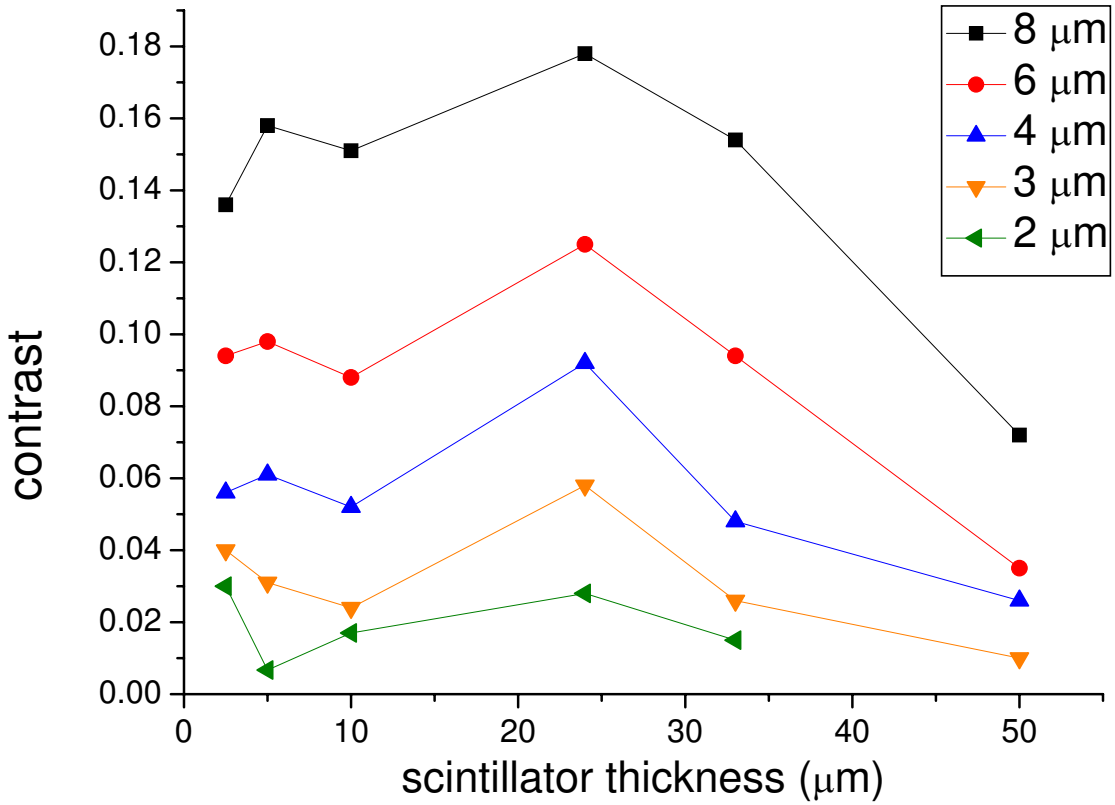

FIG. 6: [1-column-span] Influence of the thickness of the single crystal scintillator film on the contrast achievable in the image with a 10× (NA = 0.4) microscope objective (18 keV photon energy, different graphs represent results obtained by using differently sized features in the Xradia test pattern).

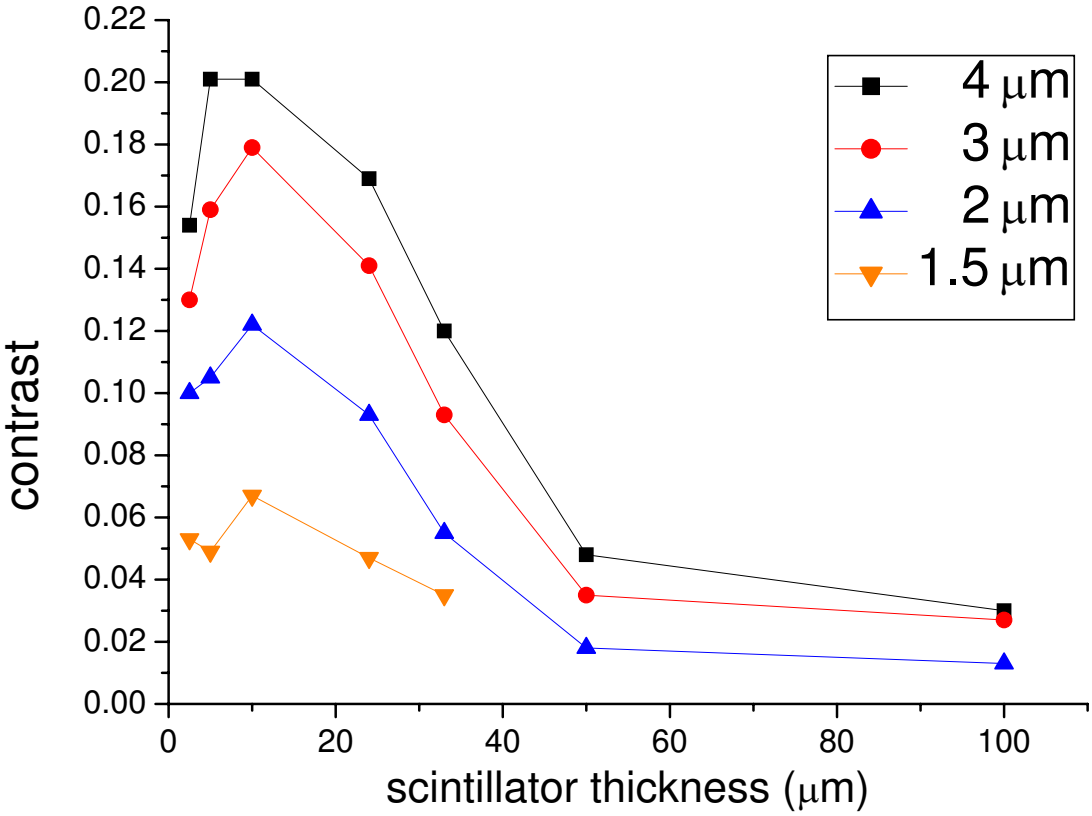

FIG. 7: [1-column-span] Influence of the thickness of the single crystal scintillator film on the contrast achievable in the image with a 20× (NA = 0.75) microscope objective (18 keV photon energy, different graphs represent results obtained by using differently sized features in the Xradia test pattern).

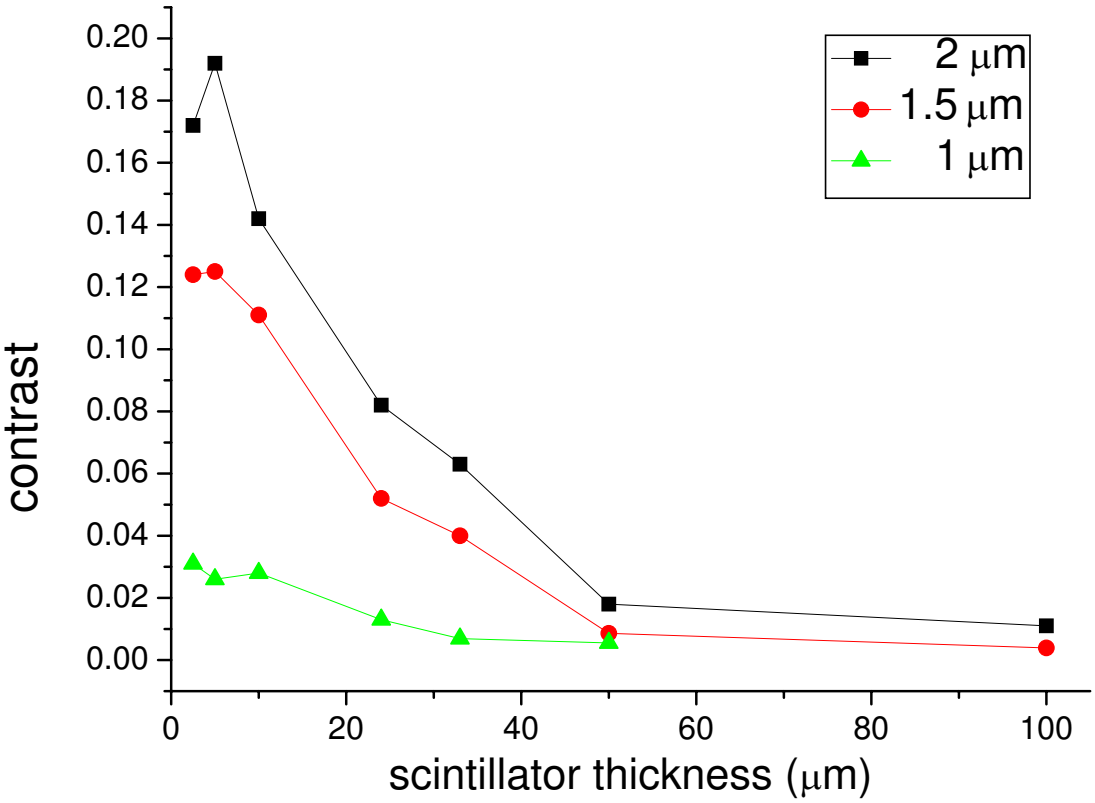

FIG. 8: [1-column-span] MTF curve at 12 keV X-ray energy measured with LSO:Tb-based scintillating thin films of different active layer thicknesses.

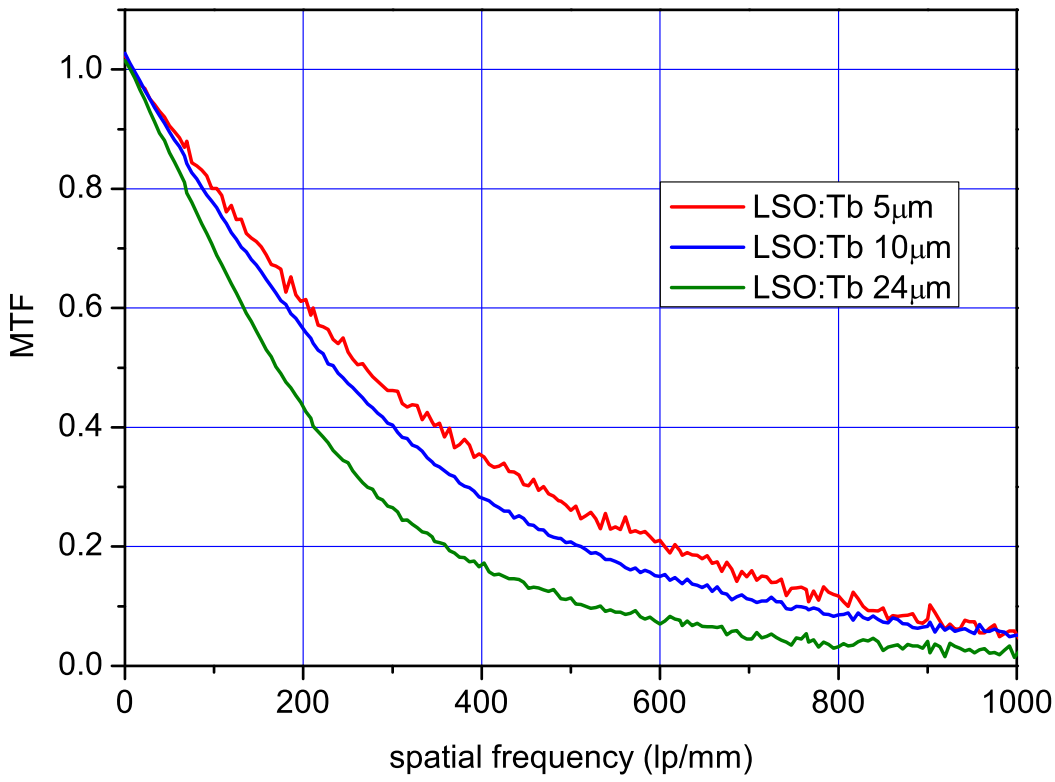

FIG. 9: [1-column-span] MTF curve at 24 keV X-ray energy measured with LSO:Tb-based scintillating thin films of different active layer thicknesses.

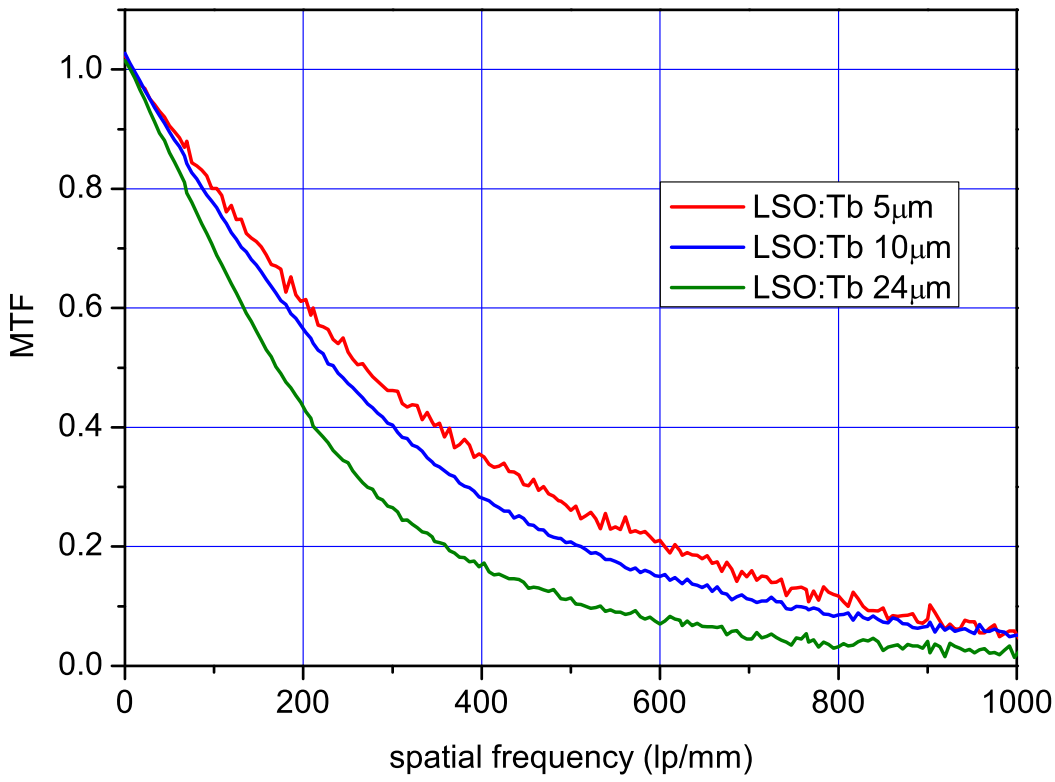

FIG. 10: [1-column-span] Top: image of a test pattern (gold, 0.5 µm line width) acquired with 0.15 µm pixel size at 2-BM (APS) using the low-dose configuration with a 20× objective (NA = 0.75), a 2.5× eyepiece and a 6 µm-thick GGG:Tb scintillator (on a GGG substrate). Bottom: representative profile plot perpendicular to the line structure: a true spatial resolution below the 1 µm-limit is demonstrated.

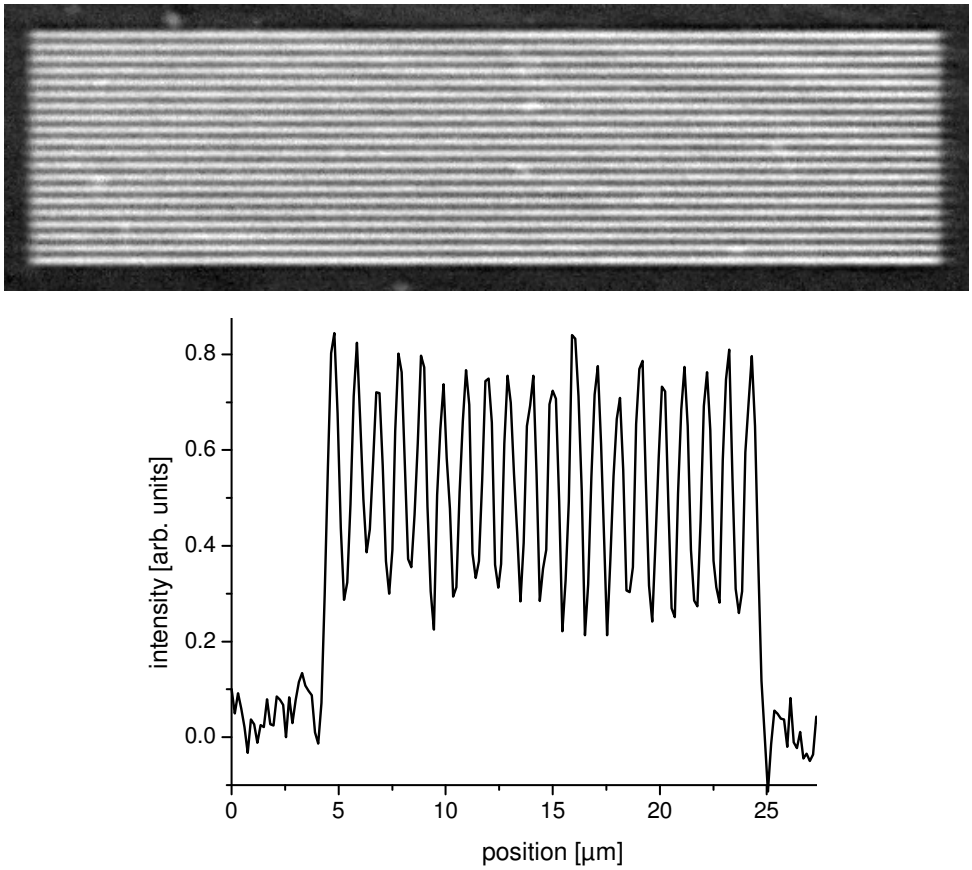

FIG. 11: [1-column-span] Top: line structure of the Xradia test pattern, acquired in white beam mode (effective pixel size equal to 0.25 µm, total magnification equal to 36×, the size of features is listed in micrometres). The cut-off frequency is marked, corresponding to a smallest distinguishable feature between 0.6 µm and 0.7 µm, i. e. a spatial resolution between 1.2 µm **(415 lp/mm)** and 1.4 µm **(355 lp/mm)**. **Bottom: overview image of the complete test pattern (acquired with 1.8 µm effective pixel size).**

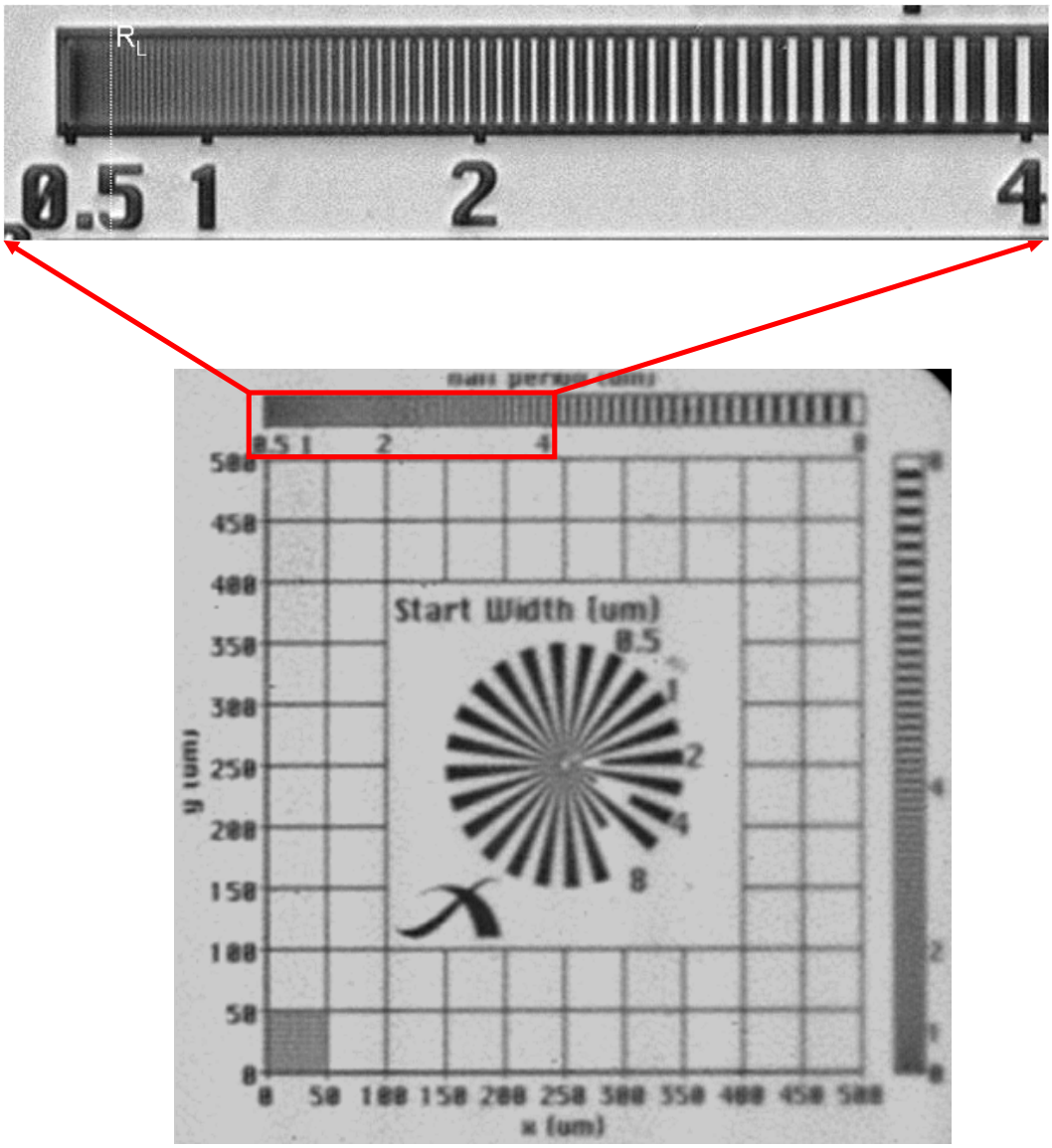

FIG. 12: [1.5-column-span] Top: tomographic slice showing a fibre-reinforced C/SiC ceramic, acquired by means of high resolution synchrotron-based microtomography. The inset shows a zoom-in with three material phases marked: Si (1), SiC (2) and C (3). Cracks throughout the sample are visible as fine black lines as well. Bottom: image of a comparable sample acquired by scanning-electron microscopy. Except for the cracks, the same phases as in the upper image have been marked.

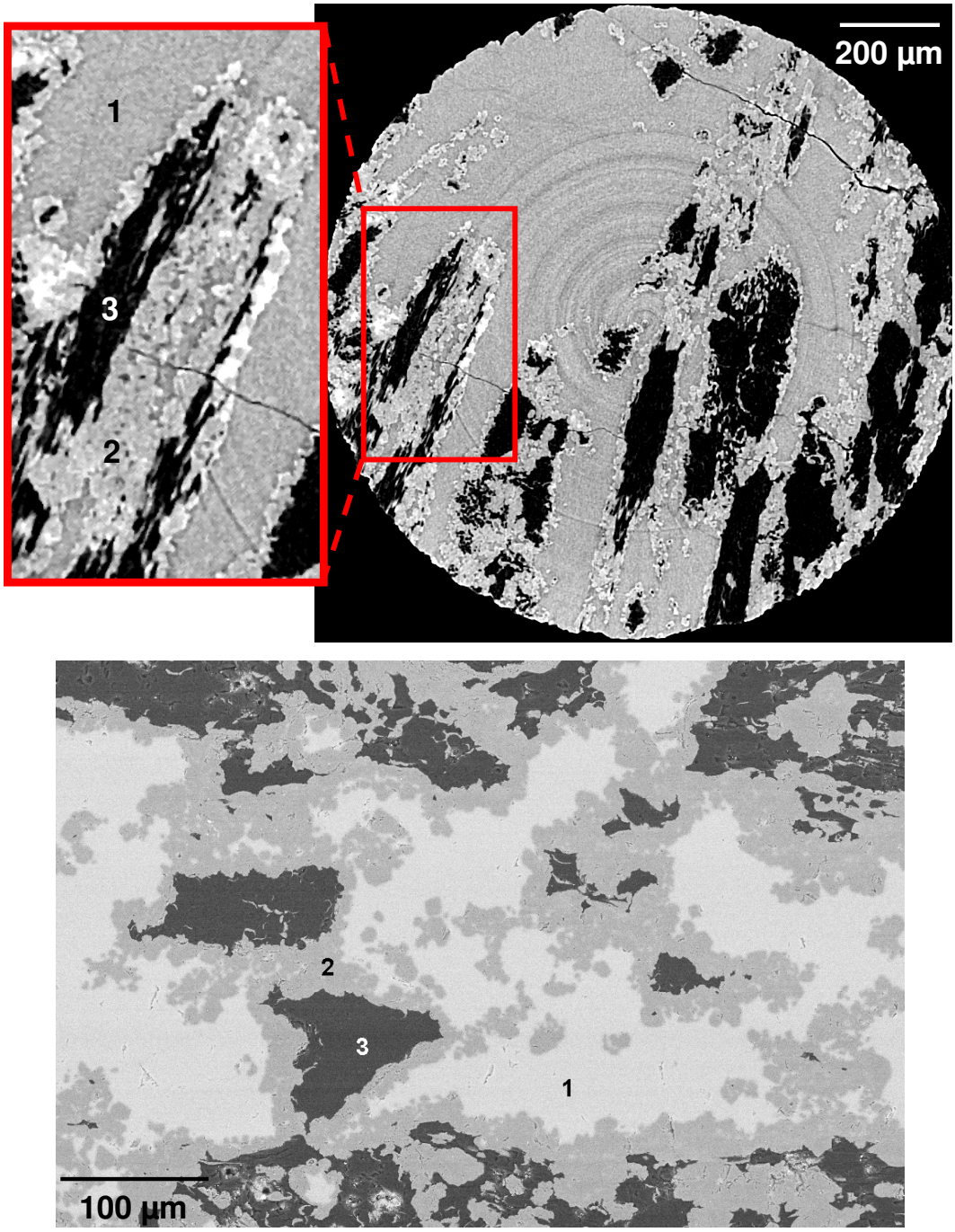

FIG. 13: [2-column-span] Time-resolved volume (4D) images acquired by synchrotron microtomography using beamline ID19 (ESRF). Depicted is a calcite rock sample during acidic attack (t0: initial condition, t30: after 28 min of attack and t70: after 66 min of attack). The white phase represents the mineral calcite phase, the orange one is the micro-porosity and the black one is the macro-porosity.

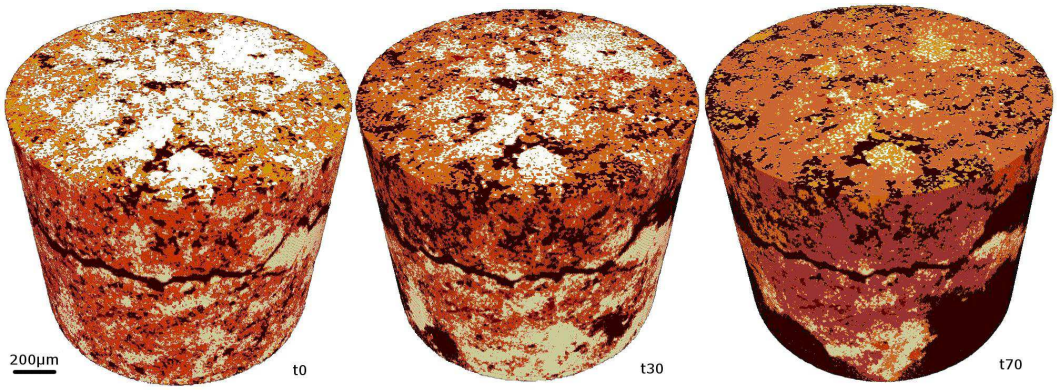

FIG. 14: [1.5-column-span] Volume rendering of a tomographic data set showing the Indonesian weevil *Trigonopterus nasutus* (acquired with white beam tomography at the ANKA beamline TopoTomo).

FIG. 15: [1.5-column-span] Virtual slice through the volume shown in Fig. 14.

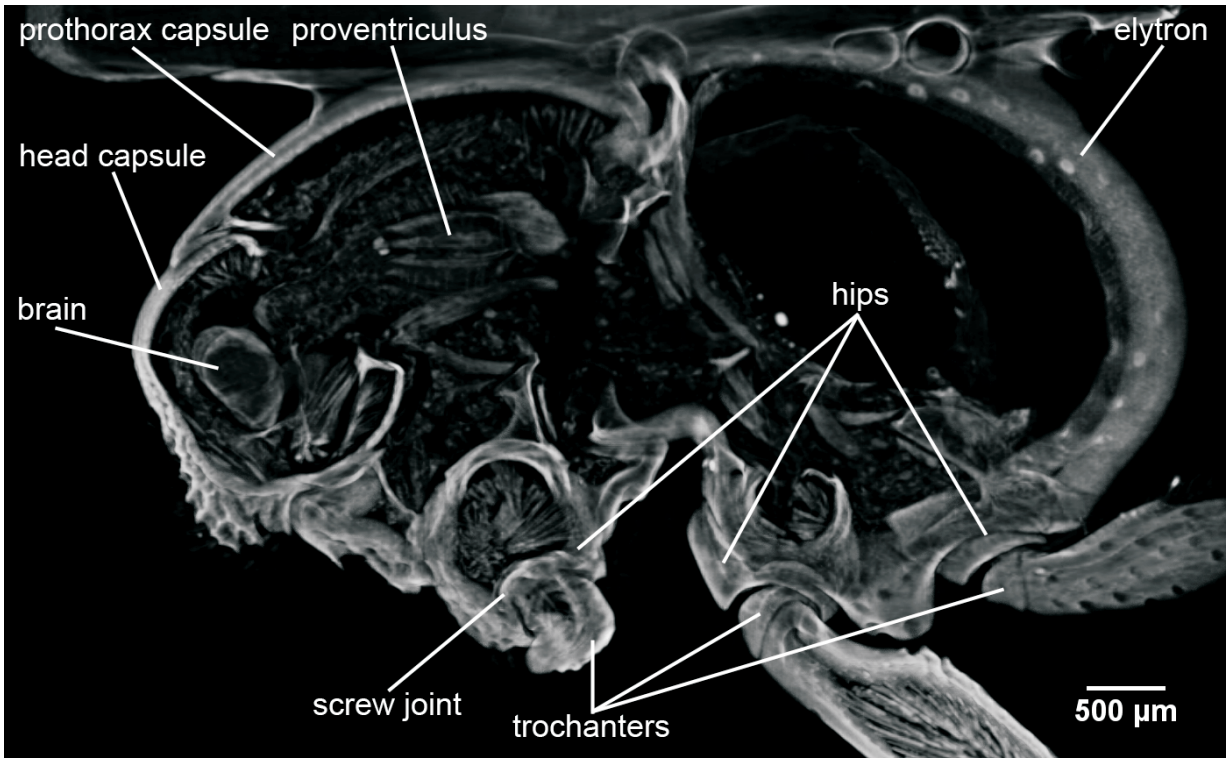

FIG. 16: [1-column-span] Cross section of a flip-chip bonded device reconstructed from synchrotron-radiation computed laminography (SRCL) data using the high-dose configuration of the microscope. The interface of the 300 µm thick bump bonds (white) towards the Cu metallisation lines (light gray) on the printed circuit board is shown. The microstructure of the metallisation as well as small voids (less than 5 µm diameter) at the bump bonds can be discerned.